Chapter 2 : Silicon detectors

This chapter briefly describes the silicon particle detectors, being either diodes or microstrip detectors, and their behaviour under exposure to radiations. Some paragraphs of this chapter were already described in previous reports [28] but are further developed here.

We start with a description of the crystal structure of the silicon bulk, putting the emphasis on the lattice orientation, which bears some impact on the detector performances. Thereafter, we continue with the depletion mechanism, crucial to understand the detection principle of a semiconductor radiation detector. We finally add the features of a segmented detector (the surface and strip parameters). The evolution of the macroscopic properties of a detector under irradiation is then outlined in a very general way since results specific to CMS structures will be discussed in chapter 4. This chapter ends with a description of the CMS detectors and the quality assurance scheme applied by the CMS sensor group these last few years.

2.1. Properties of the crystal

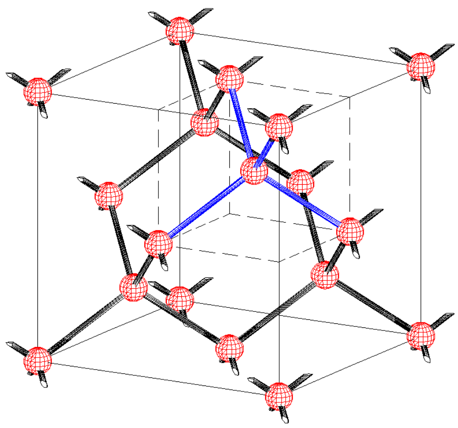

Fig. 13 : Diamond lattice structure.

The silicon crystal has the same lattice geometry as diamond, namely a face-centred cubic lattice, pictured in Fig. 13. In fact, most of the commonly used semiconductors (Silicon, Germanium, Diamond) present the same crystal geometry, but with different lattice sizes and energy gaps.

Although Silicon is very abundant on earth, it is rarely found in its crystalline form. Several crystal growth techniques have been developed to produce monocrystalline ingots, which will be used as the basic material for the production of detectors. These techniques will not be discussed here, but a good summary can be found in [32]. It is however important to mention at this point that, as the crystal is grown as an ingot, already two major characteristics of our future semiconductor detector are determined, namely the lattice orientation and the bulk resistivity.

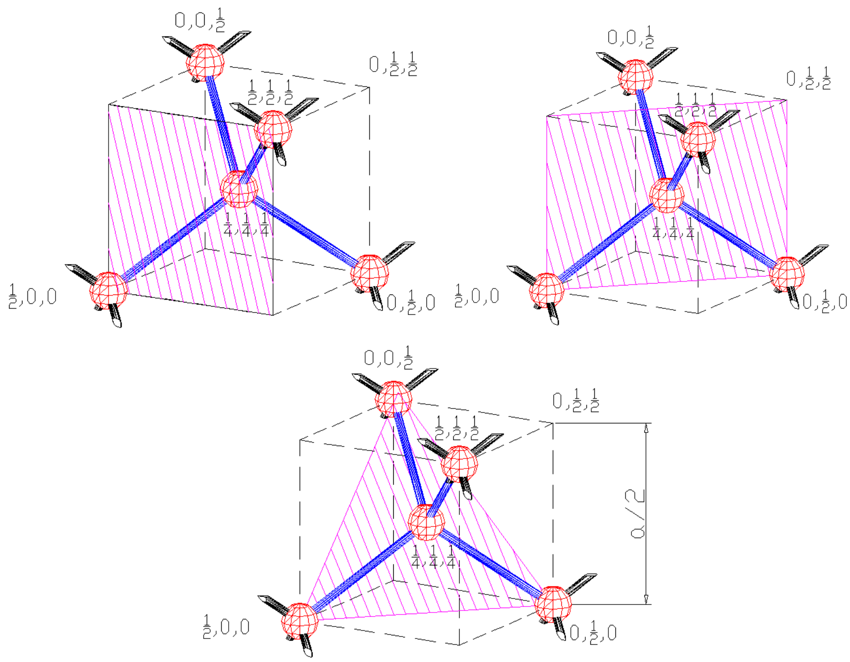

Fig. 14a, b, c: Respectively <100>, <110> an <111> lattice orientation planes (pictured in purple).

The lattice orientation of a wafer is determined by the orientation of the seed used to grow the ingot. The crystal orientation is named after the Miller indices* of the cutting plane (wafer surface). There are three possible

* The Miller indices are determined by first finding the intercepts of a plane with the three basis axes in terms of the lattice constants and then reduce these values to the smallest integers having the same ratios.

orientations for a detector, namely <100>, <110> and <111>, pictured above. One sees that the difference lies in the density of surface atoms near the cutting plane, and hence the density of unpaired electrons (dangling bonds). This will influence the surface parameters of the detector, as will be discussed when considering the CMS silicon sensors below.

The bulk resistivity (the initial concentration of defects/doping of the wafer) depends mainly on the crystal growth and purification technique. For detectors, as it needs to be as high as possible in order to reach a full depletion at a low voltage, the float zone technique seems to be the unique possibility so far as it is difficult to produce high-resistivity crystals with other techniques.

2.2. Principle of operation, characteristics

The basic principle of particle detection with semiconductor detectors is pretty similar to the ionization of a gas: a charged particle passes through the medium, exciting its constituents and creating free charge carriers that diffuse through the detector. When an electric field is applied within the detection volume, the negative charge carriers drift towards the anode (positive electrode), whereas the positive charge carriers move towards the cathode (negative electrode). Depending of the electric field, the device can also be operated in different modes (e.g. the avalanche mode), like the different regimes of a gas detector.

The comparison between gas and semiconductor detectors stops there. Big differences already arise with the nature of the charge carriers. In gas detectors, the freely moving charges are electrons stripped from the gas atoms on one side and their corresponding positive ions on the other. In semiconductor devices, if the negative charge carriers are also electrons that are relatively free to move across the lattice (with a given mobility μ_e), the positive charge carriers are not the created ions, which are locked on their lattice position. Instead, vacant positions left by electrons and created inside the lattice carry positive charges +e and are called “holes”; they can move between neighbouring atoms and behave like positively charged particles with a proper mobility μ_h. Let’s then describe the basic principle of operation of a semiconductor detector.

For this purpose, it is usual to start by a short description of doping and a discussion of the simplest yet very important P-N junction structure.

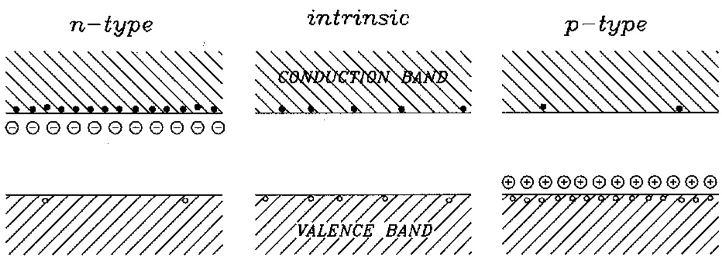

Fig. 15 : The shallow donors and acceptor levels in the band gap of silicon with the corresponding free charge carriers (from [2]).

P- and N-doped crystals are produced introducing tri- or pentavalent defects in the crystal. This raises the density of shallow donor (N-doping) or acceptor (P-doping) states which are almost always in an excited state due to their proximity to the conduction or valence band respectively (cf. Fig. 15). One then speaks of an extrinsic semiconductor. A PN junction is made by stacking a P-doped and a N-doped extrinsic crystals.

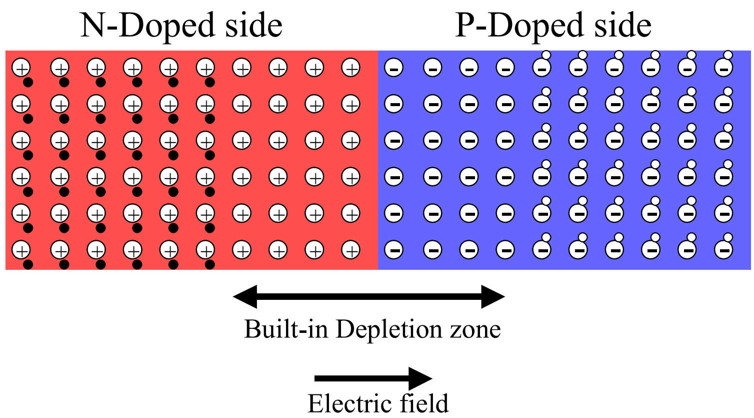

Fig. 16 : The built-in depletion zone of a PN junction and the direction of the resulting electric field.

Without the application of an external bias, such a device has free holes in the P-doped volume, and free electrons in the N-doped one. These recombine around the contact borders of the two volumes, hence creating a small built-in depletion zone (cf. Fig. 16). Initially neutral, this depletion zone becomes locally charged: one side (P-side) has a negative charge concentration, and the other side (N-side) a positive charge concentration. This depletion zone is interesting for its two main features:

1. There are no free holes or electrons, hence preventing further recombination of injected charge carriers within its volume

2. The electric field causes any charge within its volume to drift towards its borders (electrons to the N side, holes to the P side)

These two characteristics of the depletion zone are very interesting for particle detection: they prevent signal losses and help charge collection during the operation of the detector. More than this, due to recombination in undepleted areas, the depletion zone becomes the actual detection volume, it is hence standard practice to enhance the volume of the depletion zone by reverse-biasing the sensor. One generally wants to keep depleted the entire volume of the device to maximise the active thickness and to get the best signal/noise ratio.

The full depletion voltage is usually determined using the capacitance-voltage method. The boundaries of the depletion zone act like the two plates of a planar capacitance: with increasing reverse voltage (V), the distance between the planes increases and hence the bulk capacitance (C_{back}) diminishes. The relations linking the capacitance with the depletion depth is given below. A further discussion can be found in [2], [5] or even [28], we will only stress the fact that as the detector becomes fully depleted, its bulk capacitance becomes independent of the bias and a kink appears in the $1/C^2$ over voltage plot. The full depletion voltage of a planar diode is then given by (2.2).

In the following equations, q is the proton charge, ε and ε_0 define the dielectric constant, S the surface of the detector, V_{bi} is the built-in voltage and N_{eff} the effective doping concentration.

$$C_{back}(V) = \frac{dQ}{dV} = S\sqrt{\frac{q\varepsilon\varepsilon_0 |N_{eff}|}{2(V_{bi}+V)}} \qquad (2.1)$$

$$V_{dep} = \frac{q}{2\varepsilon\varepsilon_0}|N_{eff}|d^2 - V_{bi} \qquad (2.2)$$

The second main characteristics of a reverse-biased PN junction is its dark current, with a current density proportional to the depletion depth according to (2.3). The following symbols are also introduced: n_i is the intrinsic charge carrier density, τ_g the carrier generation lifetime, d_0 is the thickness of the built-in depletion zone and J_{leak} is the total dark current per unit area generated within the detector.

$$\begin{aligned} J_{leak}(V) &= -q\frac{n_i}{\tau_g}(d_{dépl} - d_{bi}) \\ &= -q\frac{n_i}{\tau_g}\sqrt{\frac{2\varepsilon\varepsilon_0}{q\left|N_{eff}\right|}}(\sqrt{V_{bi}+V} - \sqrt{V_{bi}}) \end{aligned} \qquad (2.3)$$

It is important, at this stage, to note that the ratio n_i/τ_g is also called the thermal generation rate; it is strongly dependent on the temperature and so does the leakage current according to equation (2.4) for a given bias voltage. It will be important to remember this relation when comparing the results obtained after irradiation at a temperature of –10 °C with those quoted in the literature and usually obtained at room temperature.

$$\frac{J_{leak}(T)}{J_{leak}(T_{ref})} = \left(\frac{T}{T_{ref}}\right)^2 e^{-\frac{E_{gap}}{k_B}\left(\frac{1}{T}-\frac{1}{T_{ref}}\right)} \qquad (2.4)$$

When a particle passes through a PN semiconductor device, it creates charge carriers pairs by ionizing the media. The energy required for the production of an electron-hole pair in silicon is about 3.6 eV. This is another advantage of semiconductor devices when compared to the 36 eV required on average to ionise a gas molecule. The number of generated charge carriers, as well as the Fano factor of the detection material, are crucial when considering the energy resolution of a semiconductor detector compared to any other type (the number of charge carriers being indeed the single parameter determining the statistical limit on energy resolution). We will however not discuss the energy resolution into further details here as we focus on the position sensitivity.

Indeed, the position resolution is a key element for building a tracker. The following paragraphs will hence introduce the features of a segmented silicon microstrip detector.

The two next figures show the layout of a typical CMS-silicon microstrip detector in respectively transverse and longitudinal views. Please note that we picture here only the AC-coupled version of a P^+-n-N^+ silicon detector and that there are many other sensor designs according to the wafer type, the biasing scheme and the charge carrier collection possibilities as the similar electron-hole mobilities (the saturation velocities are about 10^7 and $8.4\ 10^6$ cm.s^{-1} for electrons and holes respectively in intrinsic silicon) even lead to the opportunity to develop double-sided detectors. All these possible designs will not be discussed here since they are not used to build the CMS tracker.

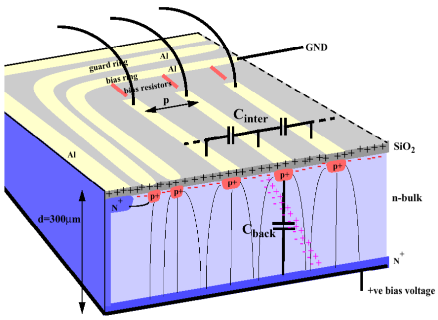

Fig. 17 : General layout of an AC-coupled microstrip detector [21].

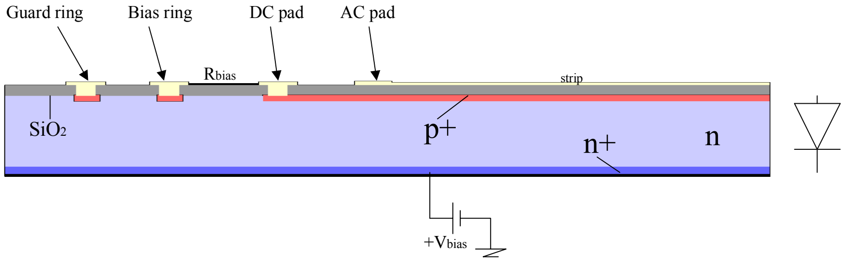

Fig. 18 : Longitudinal cut view of a silicon microstrip detector.

On the above figures, one sees the N^+ implantation, in contact to the backplane where the bias is applied. It prevents the surface current generated at the mechanical borders (cuts) of the sensor. The upper surface has the second bias contact (bias ring). The detectors are usually equipped with one or more guard rings to prevent breakdowns and leakage current between the N^+ implantation and the other surface structures due to the high voltage difference. The bias ring is connected to all strips, in this case via polysilicon resistors, to uniformly distribute a common potential and hence to define the electric field within the bulk of the detector. The resistors are in fact not connected to the surface aluminization of the strips but to the P^+ implants underneath. This is peculiar to AC-coupled detectors, where a P^+ implant forms a capacitance with the aluminization. Together with the bias resistors, these capacitances act as a high-frequency bandpass filter, allowing the acquisition system (DAQ) to react only to signal pulses without being fed by the leakage current of the detectors.

2.2.1. Charge collection and position resolution

The accuracy of the position measurement obviously depends first on the pitch of the strips. Using a digital readout, where the strip number is recorded as the crossing position of the particle, one achieves a precision of the order of $p/\sqrt{12}$, p being the strip pitch. But a higher accuracy can be reached with an analogue readout of the neighbouring strips, in which case the particle position is found by interpolation among the various strip numbers.

To assess the higher precision brought by an analogue readout, one has to have an idea of the pulse shape at the strips. Indeed, as mentioned above, when a particle passes through the detecting media and creates electron-hole pairs, these latter begin to drift within the bulk and are eventually collected either by the strips or on the backplane. The drift* of the charge carrier cloud depends on the type of the incident particle, but the pulse shape at the electrodes will not solely depend on the time spent by the charge carriers to reach the electrodes. There is also a current (i) induced on the electrodes as the electrons/holes drift towards or away of the electrodes at a given speed (v). The induced current plays a major role, and its value is given by the Shockley-Ramo theorem (2.5).

$$i = q\vec{v}.\overrightarrow{E_0} \qquad (2.5)$$

where E_0 is a function called the weighting field: it is the solution of the Poisson equation with a unit potential the concerned electrode, and 0 on every other one. A brief discussion about this theorem as well as a useful illustration can be found in [1].

In the presence of a magnetic field, the additional drift angle (called the Lorentz angle) due to the crossed electric and magnetic fields can be used to further improve the spatial resolution, as explained in ref. [15], section 2.3, in the case of the CMS pixel detector.

* A useful method to obtain a rough estimation of the width of the charge cloud to be collected by the strips can be found in [2], page 111.

2.2.2. Electrical properties of a strip detector

The leakage current of a segmented detector is correctly described by the above relations (2.3) and (2.4). Even after irradiation, the scaling of the leakage current remains valid, as will be shown in 4.2.2. But although the basic mechanism of depletion also remains the same, the capacitance-voltage behaviour is quite different. Indeed, the presence of strips at the upper surface of the detector implies a geometry of the electric field different from the one in a plane capacitor. This has been explained in a paper by E. Barberis et al. [26]. For a given effective doping concentration, a segmented detector will show a higher depletion voltage compared to a diode according to:

$$V_{dep,seg} = V_{dep,diode}\left[1 + 2\frac{p}{d} f\left(\frac{w}{p}\right)\right] \qquad (2.6)$$

where p is the pitch of the strip, d is the detector thickness and w is the strip width; *f*(w/p) is a function whose details are given in the above-mentioned article. The diode depletion voltage can be determined using equation (2.2).

It is important to note that the method for determining the full depletion voltage is not affected in any way by the segmentation of the detector: the plot of $1/C^2$ as a function of bias will also show the characteristic kink of the depletion voltage of the device. However, we will have to take this effect into account when using either the depletion voltage to determine the effective doping concentration, or its evolution under irradiation to compute the changes in full depletion voltage.

In addition to the bulk properties, a segmented detector has many surface characteristics that are of major importance when considering the overall performance of the device.

1. Coupling capacitances are a key element in charge collection. Their value should be as high as achievable to ensure a good charge transmission to the readout electronics.

2. Interstrip capacitances are the major contributor to the crosstalk between strips and noise. Interstrip capacitances can be used to improve the position accuracy in the case of a capacitive charge division readout. However high interstrip capacitances may cause deviations from linearity of the charge division between

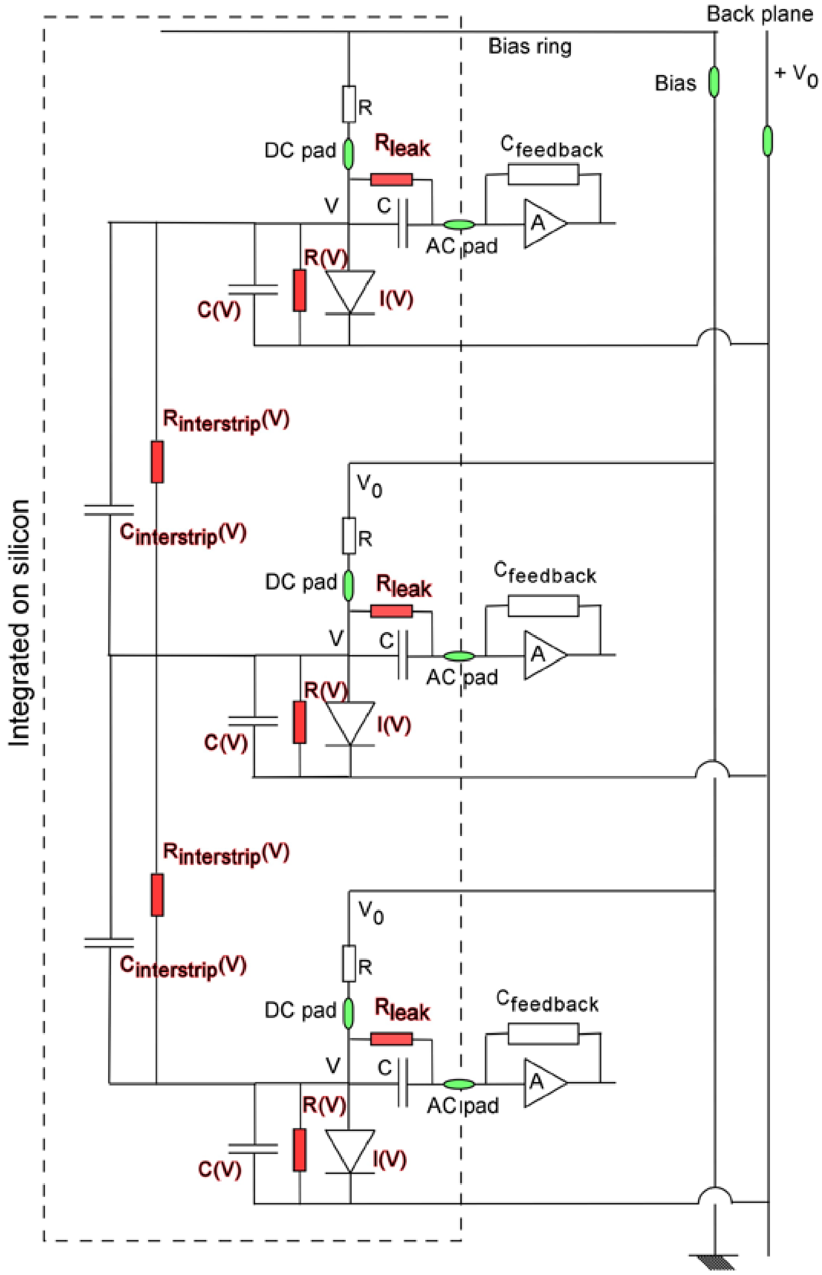

Fig. 19 : Circuit diagram of a silicon microstrip sensor.

two adjacent strips and generate in some cases a position-dependent accuracy. Interstrip resistances mainly contribute to the noise if their values are too low, hence also deteriorating the performance of the sensor.

3. Bias resistors have to be as uniform as possible across the device to ensure a uniform electric field within the bulk. Especially after irradiation, when the leakage current is high..

4. The overall surface quality of the sensor also plays a major role. For instance, a poor surface quality or a breakdown of the superficial oxide layer may lead to "pinholes". These are pictured as R_{leak} through which currents collected at the P^+ implant directly leak into the readout electronics, ruining all the advantages of an integrated AC-coupling.

The S/N ratio of a detector module depends not only on the sensor, but also on the readout electronics. Some general considerations regarding the noise of an AC-coupled detector can be derived from the electrical scheme pictured in Fig. 19:

1. Thermal noise: it is due to the thermal fluctuation of charge carriers present in the bulk, and proportional to $\sqrt{4kT/R_{poly}}$. Hence, the sensor should have high values of the bias resistor, but without compromising the field uniformity across the surface of the sensor.

2. Shot noise: the shot noise is due to the fact that the charge is quantified. In this case, noise is proportional to $\sqrt{2qI_{leak}}$.

3. Serial noise: Serial noise find its source in the readout amplifier and depends on its transfer function. It adds in quadrature to the thermal noise, and its value is proportional to sum of the capacitances seen from the input of the amplifier: the capacitive feedback of the amplifier ($C_{feedback}$) and the total strip capacitance composed of the coupling capacitance (C_{AC}), the interstrip capacitance (C_{int}) and the strip bulk capacitance (C_{bulk}).

4. Low-frequency noise: The origin of low-frequency noise, or Flicker noise, in detectors [30], and silicon devices in particular [31], is still not well-known. Empirical models exists, that show

that above a given frequency, pure white noise (thermal and shot noise) is observed.

More details about noise in detectors can be found in either [2], [29]or [30]. Very important results about the S/N ratio of a detector and its related electronics can be obtained by means of numerical simulations. In the case of CMS sensors, these have been reported in [33] and will be summarised later in the discussion about the design of the sensors.

About the surface parameters, the lattice orientation and number of dangling bonds play another essential role. Even though there are only little differences between <111> and <100> brand new devices, the lattice orientation: as a general rule, a low surface density of dangling bonds is an asset for the radiation hardness.

Despite the fact that the effects of the surface parameters on the detector performances have known tendencies, there are no general rules or recipe to design a detector: these considerations on the surface parameters of a sensor stress the importance of simulations and prototyping of the devices before any mass production. Highly critical in the case of the CMS tracker, this development phase is outlined in 2.4.

In addition to the stringent requirements on these parameters, it should also be stressed that all measurements of these characteristics should be performed in perfectly well-defined conditions. For instance, as a segmented detector is a complex network of resistances and capacitances, the frequency used by the LCR-meter to determine the capacitances plays a major role in the reproducibility of the results. The measurement of the interstrip resistances has also to take into account the depletion state of the sensor because the electric field near the surface plays a major role in the concentration of charge carriers nearby the strips. To cope with this issue in the context of the CMS QA scheme, a very detailed protocol has been fixed by the collaboration

2.3. Radiation-induced changes in detector properties

This section outlines the evolution of a silicon detector properties under irradiation. It is inspired from ref. [2] and [32], which are standard references in the domain.

2.3.1. Basic damage process

The very first damage process in the bulk is the creation of a Frenkel pair in the crystal lattice due to a primary knock on atom*. Being either light or heavy, charged or not, the incident particle kicks a silicon atom out of its position within the lattice, creating a vacancy-interstitial pair. The threshold for this process is 25 eV. Once knocked out of its position, the silicon atom can in turn, if energetic enough, create other defects on its own in a cascade process. The high concentrations of defects caused in this way are often called "clusters"**, as opposed to point defects caused along the track of an incident particle, as depicted in Fig. 20.

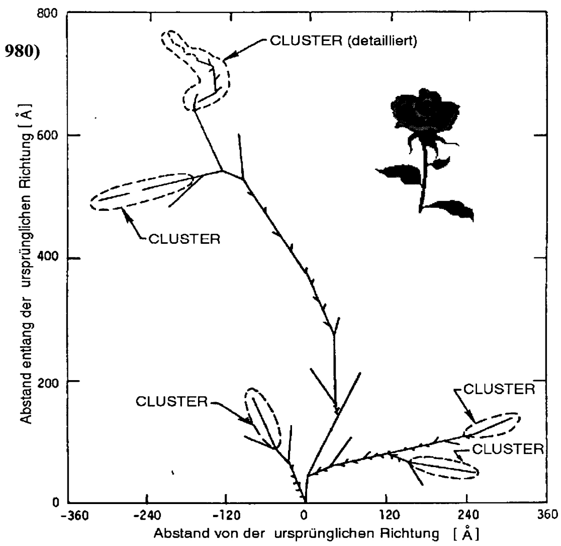

Fig. 20 : Basic damage cascade process caused after a PKA: the initial impact took place at location (0,0). Taken from the ROSE collaboration, [32].

Once created, all these primary defects move within the silicon bulk through a diffusion process and are likely to recombine in many different stable defects, inducing now irreversible damage which influence permanently the macroscopic properties of the detector. The reaction rate at

* Often referred as PKA.

** The defect concentration is computed to be as high as 100 defects in a 5 nm diameter volume.

which this process takes place is highly dependent on the temperature because of the defect mobility within the bulk of the sensor.

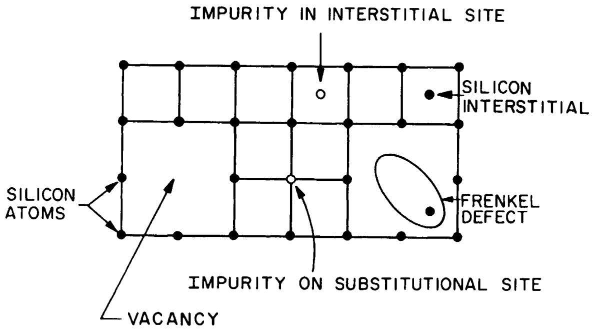

Fig. 21 : Simple defects in a 2-D crystal, from ref. [2].

There is an extensive nomenclature of these defects, based on the combination of simple defects such as vacancies (V), silicon interstitials (I), impurities (for which the symbol taken is often the chemical symbol of the interstitial atom), as described in Fig. 21.

These permanent defects are in fact recombination centres acting as electron or holes traps depending where their energy level lies inside the band gap. From a macroscopic point of view, the defects generate higher leakage current, modify the depletion voltage (changing the effective doping concentration) and diminish the charge collection efficiency by trapping either the electrons or holes created by the ionizing incident particle.

A further interpretation of the link between microscopic defects and macroscopic properties requires first to describe the evolution of these.

2.3.2. The NIEL hypothesis

Despite the complexity of reactions taking place in a semiconductor device when exposed to high radiation levels, first studies have demonstrated that the evolution of some macroscopic characteristics can be described using a relatively simple hypothesis: the NIEL* hypothesis according to which only the non-ionizing component of the total energy deposit within the device contributes to permanent damages. The spatial extension of the reaction cascade, as described above, and the complexity of the lattice perturbations are not taken into account.

* NIEL: Non-Ionizing Energy Loss.

The evaluation of the non-ionizing component is made by computing D, the displacement cross-section, also called the average displacement KERMA. For a given particle flux, this is done according to the following definition of a flux-weighted cross section (2.7):

$$D = \frac{\int_E \frac{d\Phi(E)}{dE} D(E) dE}{\int_E \frac{d\Phi(E)}{dE} dE} = \frac{\int_E \frac{d\Phi(E)}{dE} D(E) dE}{\Phi_{tot}} \qquad (2.7)$$

Where

$$D(E) = \sum_k \sigma_k(E) \int dE_r f_k(E, E_r) P(E_r) \qquad (2.8)$$

The last equation (2.8) is the expression of a macroscopic interaction cross section (or "damage function") for a given particle interacting through different reactions within the device, $\sigma_k(E)$ being the cross sections of these reactions ; $f_k(E, E_r)$, the probability for an incident particle of energy E to produce a recoil energy E_r in a reaction of type k while the function $P(E_r)$ is the part of the recoil energy E_r deposited in displacements.

Expressed in MeVmb, this quantity D is usually normalized to the displacement cross section for damages produced by a 1 MeV neutron, quoted to be 95 MeVmb[¤]. The subsequent factor is then referred as κ, the hardness factor of the radiation field. It is then used to compare, scale and add fluences of different particle types and energies.

$$\kappa = \frac{D}{95 MeVmb} = \frac{\int_E \frac{d\Phi(E)}{dE} \kappa(E) dE}{\Phi_{tot}} \qquad (2.9)$$

[¤] 95 MeVmb is the value of the displacement function for 1 MeV neutrons, and is the most commonly used reference value although some rather use a value of 76.9 MeVmb which averages a bit around 1 MeV, because the displacement cross sections varies a lot in the vicinity this neutron energy (cf. [40]).

Where

$$\kappa(E) = \frac{D(E)}{95MeVmb} \quad (2.10)$$

On the basis of this normalisation, a "real" particle fluence is expressed in its "1-MeV neutron" equivalent using (2.11):

$$\Phi_{eq} = \kappa\Phi_{tot} \quad (2.11)$$

Compilations of the hardness factors can be found in references [22], [41] and [42]. Neutron coefficients taken from these references are illustrated in Fig. 22.

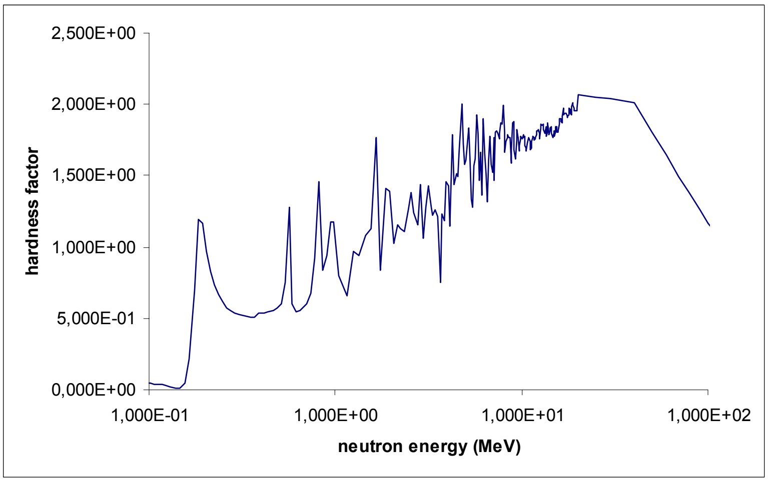

Fig. 22 : NIEL hardness factors in the case of neutrons from 0.1 to 100 MeV.

M. Huhtinen performed this normalization in the case of the radiation field present in the CMS tracker during its operation in [15], and updated it in [16]. This has been outlined in 1.2.2.

The success of this approximation is based on the fact that the strong dependence on particle type and energy of the interaction is smoothed out to a large extent by secondary reactions within the displacement cascade [2]. It therefore provides a good scheme to predict the evolution of the leakage current of a detector but failed however to explain various aspects of the changes in the macroscopic properties of the detector, such as the reverse annealing of the depletion voltage. The latter still requires further investigations on the microscopic defects produced during irradiation. This is illustrated by the fact that oxygenated silicon detectors are less subject to damage when exposed to the same 1-MeV equivalent fluence of protons than when exposed to neutrons.

2.3.3. Evolution of detector properties

Now that the basic processes of damage within a semiconductor sensor have been shortly discussed, it is time to consider how they affect the macroscopic properties and the functionality of the detector. The bulk parameters such as leakage current and depletion voltages are the most affected characteristics of the sensor and will be addressed first. The surface structures will be discussed thereafter.

2.3.3.a. Leakage current

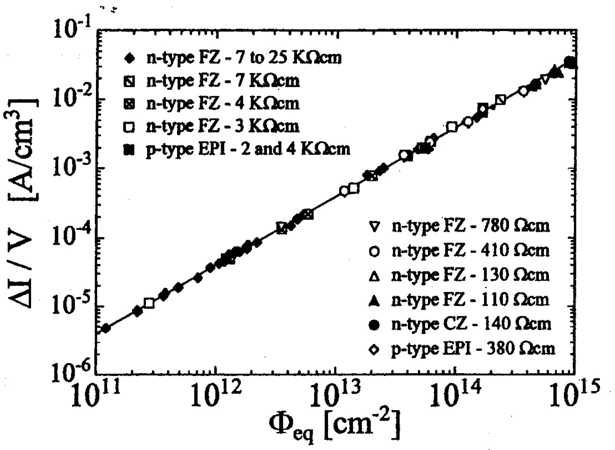

Fig. 23 : Increase of the leakage current density as a function of the fluence, measurements performed after 80 minutes of annealing at 60 °C (taken from [32]).

For a long time now, it has been shown that the leakage current increases linearly with the 1-MeV equivalent fluence (Fig. 23). This effect has been found to be material-independent (manufacturing process, initial doping concentration, p or n-type) and particle-independent (irradiations with neutrons or charged particle).

It has been mentioned above that the frenkel pairs, initially created by PKA, are mobile within the bulk and recombine to create stable defects. It is then no surprise that the electrical properties of a sensor further evolve after irradiation, even if not submitted to any additional fluence. In the case of the leakage current, the same annealing behaviour is observed for all detector materials and all particle types. Although the time constants for this annealing highly depend on the annealing temperature (Fig. 24), the current increase rate is hence found to be the characteristic which best follows the NIEL hypothesis for any incident particle type.

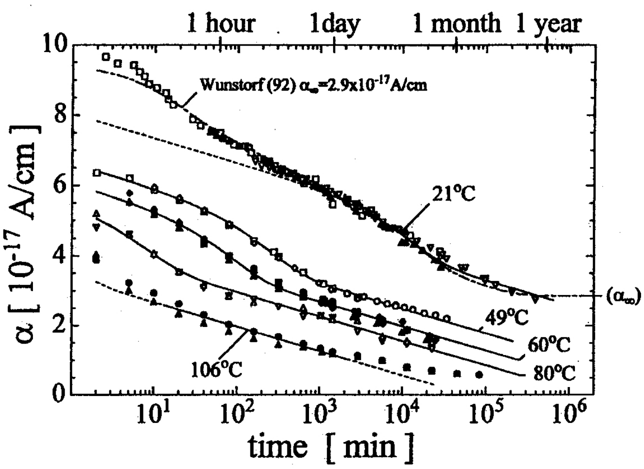

Fig. 24 : Leakage current annealing behaviour after irradiation: α is the leakage current of the detector divided by its volume times the 1-MeV equivalent fluence it has been submitted to (from [32]).

As a consequence of the annealing behaviour, the measurements of the leakage current after irradiation have to be made within careful conditions, to allow further comparisons. This is an additional constraint on the post-irradiation tests in order to ensure the reproducibility of the results. From the leakage current point of view, a 15-day annealing at room temperature (21 °C) is equivalent to 80 minutes at 60 °C. This standard annealing step, widely used in literature, will also be performed for the CMS tests.

2.3.3.b. Depletion voltage

Compared to the leakage current, things get more complicated when considering the depletion voltage. Indeed, the effective doping concentration does not present a simple linear evolution with the fluence combined with a beneficial annealing afterwards. Considering a n-type bulk, the damage behaviour presents rather a combination of exponential decrease of the initial donor concentration, combined with a fluence-proportional damage that anneals both beneficially and adversely.

The current parameterization of this evolution is known as the Hamburg model, developed by the RD48 collaboration. It uses the NIEL hypothesis as a starting point, but classifies bulk damages in four categories, as mentioned above:

1. The first effect of radiation is an apparent donor removal, the donor removal rate being proportional to the donor concentration, this contribution has an inverse exponential form;

2. The introduction of stable damage is proportional to the fluence, and quantified by an introduction rate g_c;

3. g_a quantifies the introduction of damage that will beneficially anneal out. This annealing also presents an exponential time dependence whose time constant depends on the temperature at which the device is stored. For instance, the time constant vary from about a year at –10 °C, down to 2 minutes at 80 °C.

4. The last term is the reverse annealing contribution to damage. The introduction rate is noted g_Y and the time dependence also depends on the temperature: from several hundreds of years at –10 °C to around 92 minutes at 80 °C.

Equation (2.12) gives the whole picture of the Hamburg model, with all effects and including annealing. One can distinguish the various terms in the same order as mentioned above, with the first term representing the initial doping concentration minus the donor removal and the second term representing the fluence-proportional contributions of stable damage, beneficial annealing and finally reverse annealing.

$$N_{eff}(\Phi_{eq}, t_a, T_a) = N_{eff,0}\left(1 - r(1 - e^{-c\Phi_{eq}})\right) - \Phi_{eq}\left(g_c + g_a e^{-\frac{t_a}{\tau_{T_a}}} + g_y(1 - e^{-k_{T_a} t_a})\right) \qquad (2.12)$$

The dose evolution of this relation is pictured in Fig. 25 whereas Fig. 26 illustrates the temperature annealing.

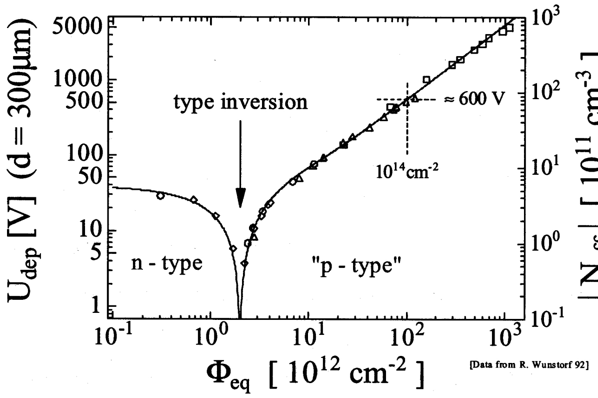

Fig. 25 : Typical evolution of the effective doping concentration of a n-type initial bulk, as a function of the fluence, for a given annealing state. From ref [32].

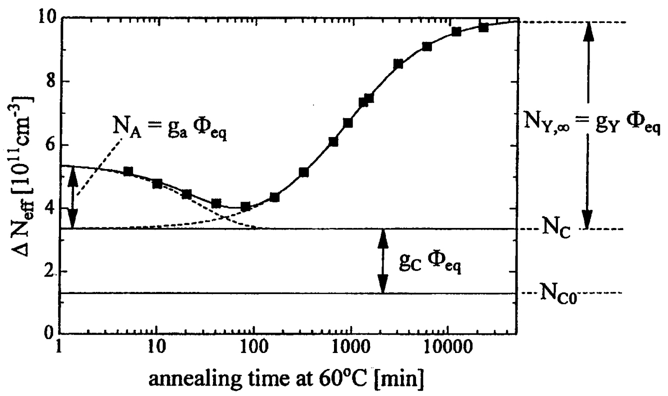

Fig. 26 : General scheme of the post-irradiation effective doping concentration evolution under annealing. From ref [32].

A compilation of all the experimental time constants can be found in [32].

The behaviour of the depletion voltage of a detector under irradiation puts an emphasis on the limitations of the NIEL hypothesis. Indeed, here the effective doping concentration does not present the same evolution for all materials and particle types. One of the most striking effect is the proton-neutron puzzle: for the same initial resistivity, an oxygenated detector will show a higher resistance to neutron fluences, compared to a non-oxygenated one. This effect isn't observed if both detectors are irradiated with protons.

Hence, the NIEL hypothesis is still useful if one knows how a given material reacts to radiations, but a more fundamental approach based on the study of the microscopic defects induced within the bulk has to be used if one wants to know what happens. Such studies, requiring instruments such as deep level transient spectroscopy (DLTS) or thermally stimulated current (TSC) are being carried out by e.g. the RD50 collaboration.

2.3.3.c. Surface structures

All the properties studied so far are bulk properties of the detector. Surface properties, also affected by radiation are critical regarding the detector operation. The trapped charges at the crystal boundaries play indeed an important role as far as resistances and capacitances are concerned. But the surface of the detector is, in most cases, covered by an insulator (SiO_2) and it can hence no longer be considered as a semiconductor crystal.

The damage mechanism is a bit different within an oxide: displacement damage is not the only permanent effect anymore and ionization comes in front of the scene. First, it is important to notice that the band gap is higher for an insulator (for SiO_2 for instance it is 8.8 eV): the emission of captured charge to the conduction band is therefore almost impossible. Then, the crystal/oxide region is a high defect density zone, and charge trapping by this defects plays an important role. Also, the mobility of electrons and holes are very different for insulators. All these effects combined have, as a consequence, that radiations can change the charge state of the insulator.

A consequence of this is that highly-penetrating particles (e.g. neutrons) produce less ionization and hence cause less surface damage than short range ones (X-rays, charged particles). Protons for instance affect more the surface of a detector than neutrons, and this has been seen during the CMS tests when comparing the radiation damage caused by protons in Karlsruhe with the neutron damage caused in Louvain-la-Neuve. This is a further argument for the above-stated complementarity of neutron and proton irradiations

But, besides this qualitative interpretation of damage at the detector surface, there are only few studies about the evolution of the surface structures of microstrip detectors under heavy irradiation. And it is difficult to foresee how these structures will evolve in a quantitative way. One of the reasons for this is that segmented detectors show a wide variety of designs, and hence it is difficult to disentangle general trends for modelling the evolutions under irradiation. Also, in many cases, these structures are, in fact, only slightly affected by irradiation. A study of the evolution of the surface parameters of the CMS sensors under neutron irradiation is carried out in chapter 4. The bad news are that in general the variations go in the way of a deterioration of the performances of the detector (bias resistors, interstrip resistances and coupling capacitances decrease whereas interstrip capacitances increase); the good news being that these variations leave the sensors within the specifications for a good tracking performance.

2.3.4. Correlations between microscopic defects and macroscopic properties

This work focuses on the evolution of the macroscopic properties of a silicon microstrip sensor under irradiation. But, as the annealing picture for both the leakage current and the effective doping concentration have been described, it is now interesting to give a short summary of what is the microscopic picture, and what could be the links between both.

At the microscopic level, impurities are named upon the atoms and type of defects they involve. From the electrical properties point of view, neutral defects have no influence on the semiconductor. This is the case for some combinations involving carbon atoms, whether on a lattice node or not.

Electrically charged defects are energy states located within the band gap. Like for the initial doping, these states can be close to the conduction or valence band (shallow defects). At the contrary, deep levels are close to the midgap.

The concentrations of defects as a function of the detector's annealing state have been studied in careful studies. They have pointed towards the fact that some of these affect the leakage current, whereas others affect the depletion voltage.

For instance, a very good candidate to be responsible for the leakage current increase is the divacancy (VV) and some of divacancy-related defects. This could explain:

- Why the alpha parameter does not depend on the bulk material type: divacancies are the dominant primary defects, depending on the lattice deterioration and not on a subsequent recombination.

- Why the leakage current shows only beneficial annealing: divacancies are very likely to recombine with other impurities or interstitial atoms: the concentration of divacancies can only drop, and hence the leakage current. The annealing curve could then adequately be described by means a sum of decreasing exponentials, each describing the different recombination possibilities for divacancies.

As far as the effective doping concentration is concerned, new microscopic candidates appear. For instance, the V_2O defect. As a complex defect made of a divacancy and an oxygen impurity in the bulk, it can be formed after irradiation. Such recombination mechanisms are thought to be the source for the following effects:

- Reverse annealing of the effective doping concentration: during beneficial annealing, primary defects concentration drop, whereas the reverse annealing, due to less probable recombinations, takes longer.

But a detailed knowledge of the microscopic evolution can also put some light on effects that cannot be explained by the simple NIEL picture:

- the so-called “proton-neutron” puzzle in oxygenated detectors. Oxygenated detectors have shown lower post-irradiation depletion voltages than standard silicon ones when irradiated by a proton flux. This could be explained by the different distribution of primary defects within the bulk for proton/neutron irradiations. Neutron irradiation produces mainly concentrated clusters, as opposed to proton irradiation where primary defects are spread along the entire particle track. This difference in initial defect concentrations can lead to different microscopic kinetics: the production of the electrically inactive V_2O_2 could be enhanced to the detriment of V_2O in the case of proton irradiation.

In the case of the CMS Irradiation Quality tests programme, the experimental result have demonstrated that standard silicon shows the same behaviour under proton and neutron irradiations. But still, this short summary stresses one more time that it is essential that both types of irradiations are performed for monitoring the radiation hardness of the CMS silicon sensors.

Furthermore, if there was the need for an additional argument in that sense: another major difference arises when considering the surface damage. Surface structures are less affected by radiations than the bulk of the sensor, but the damage mechanism is believed to be of a completely different origin as surface damage is mainly due to trapped charge and hence ionization, as opposed to non-ionization for the bulk. A proton irradiation will for sure induce a lot of ionization on the surface, whereas neutrons not.

2.3.5. Comments on bias and irradiation rate

A frequent question about radiation hardness tests to study the survival of detectors in a harsh environment is the influence of the dose rate. Is a fast irradiation performed inside a nuclear reactor or near an accelerator really equivalent to a 10-year operation at the LHC?

Whereas there is no detailed study yet about the flux dependence of strip parameter damage, irradiations have been carried out by a Slovenian group to study the impact of flux on bulk damage [34]. Their conclusions mainly deal with the full depletion voltage: it is found to be flux-independent over a wide range of fluxes from $2\ 10^{8}$ to $5\ 10^{15}$ $n/cm^{2}s$ for the same integrated fluence.

The bias-dependence of the damage is another important question related to the irradiation tests. Indeed, the high fluxes used during radiation hardness tests usually prevent the biasing of the devices during the irradiation themselves, whereas they will obviously be biased during operation at LHC. One can intuitively imagine that any electric field within the bulk of a detector may have an impact on the electrically charged defects and their kinematics.

Very few studies of the impact of biasing during irradiation have been carried out so far, among these the study performed at Lubljana (Cindro et al [35] and [36]), Mikuz et al [37]). Their main conclusions show an effective dependence of the damage on the bias. Although the leakage current seems unaffected, the full depletion voltage tends to increase when structures are biased:

- Right after irradiation, the biased diodes (those that were kept biased) exhibit a much higher depletion voltage than the other ones.
- This difference tends to vanish on diodes on which bias is switched off (after ~100h).
- Also, samples that were kept unbiased during irradiation show an increasing V_{dep} when kept biased for a long time. Hence, both the diode samples that have been biased and unbiased during irradiation exhibit this effect.

This increase of the depletion voltage is thought to come from a bistable defect, which is introduced in the structure whether biased or not during irradiation. The study estimates its impact to be as high as 80 V at the end of the detector lifetime.

The influence of bias in the case of our tests within CMS will be discussed and compared to these results in 4.2.1.

2.4. CMS sensors designs

The construction of the CMS tracker requires many different detector designs to fulfil the resolution requirements and ensure a uniform evolution of the electrical properties of the detectors under the radiation field. To design all these geometries, a series of multi-geometry detectors have been fabricated [38].

As a starting point, the well-known and generally used P^+-n-N^+ scheme has been kept, with an integrated AC-coupling and a polysilicon resistor-biasing scheme (cf. Fig. 17, above).

The other parameters like capacitance, crystal orientation or initial wafer resistivity had to be studied further to ensure the reliability and lifetime of the detectors in the LHC environment. The specific R&D will not be fully described here as it is not part of our work, but the main results will be briefly discussed since they have implications on the design of the tracker and the results of irradiation tests.

A CMS R&D study [38] has been carried out on specific structures that have different pitch values, covering the range foreseen for the tracker, and which have various implantation width over pitch ratio. Each of these structures has been produced with different crystal orientations and initial resistivity. Some of these test sensors have been exposed in the CERN PS irradiation facility with 24 GeV protons for radiation hardness testing.

The pitch (p) and strip implantation width (w) interplay and have an impact on the backplane and interstrip capacitances. With irradiation, the backplane capacitance is found to decrease whereas the interstrip capacitance increases. This increase is a function of w/p only. The ratio w/p has been subsequently tuned to minimize the variation of the total strip capacitance (backplane+interstrip) variation. This is a major result as numerical simulations of the sensors have shown that this strip capacitance is the key feature for the noise of the detector : it dominates the serial noise discussed above. As a further consequence, for modules composed of 2 daisy-chained sensors, it implies that the resulting noise will also increase, requiring the thickness of these sensors to be increased. This is the reason why you have thicker sensors in the outer part of the tracker.

The performances of <111> and <100> oriented substrates have also been compared. Although they were similar before the radiation tests, the interstrip capacitances of <111> ones raises more with fluence than the other, as reported in [33]. This result is highly dependent on the bias voltage and operation frequency of the LCR meter, but is one of the main reasons to choose the <100> orientation. As mentioned above, it is thought to be due to the amount of dangling bonds (atoms at the surface of the silicon wafer), which is smaller in this particular orientation.

The depletion voltage is initially determined by the resistivity[¤] and the thickness of the wafer: the higher the resistivity, the lower the depletion voltage; the higher the thickness, the higher the depletion voltage. One might therefore consider the use of the highest achievable resistivity, but this will make the biasing easy only at the beginning of detector's lifetime, as the bulk type inversion process will occur soon in the radiative environment encountered at the LHC. Indeed, with a detector built on a very high resistivity wafer, we would end up with higher biasing needs due to the subsequent rise of the depletion voltage. The problem of the bulk type inversion is even more important as the junction moves from the front to the backplane; hence the detector needs to be always fully depleted to avoid the recombination of charge carriers and signal losses. Therefore, the initial resistivity of the wafers has to be carefully chosen in order to get final depletion voltages similar to the initial ones. This is done using simulations of the radiation field at the LHC, normalizing it with the NIEL approximation and applying the Hamburg model to take into account the variations in effective doping concentration and thermal annealing effects during the maintenance periods[*]. A typical example of such simulation is pictured on Fig. 27. To cope with this issue when building the CMS tracker, it has been divided into 2 volumes, inner and outer ones, with different resistivities and thicknesses (1.5-3 kΩ.cm and 320 μm for the inner part, >4

[¤] The resistivity is linked to the effective doping concentration according to the relation $\rho = \dfrac{1}{eN_{eff}\mu}$

[*] It is often assumed that the CMS tracker will be kept cold at –10 °C all year long, excepted for an annual period of 30 days at higher temperature for maintenance.

kΩ.cm and 500 μm in the outer zone) to keep the uniformity of biasing as constant as possible across the whole sub detector.

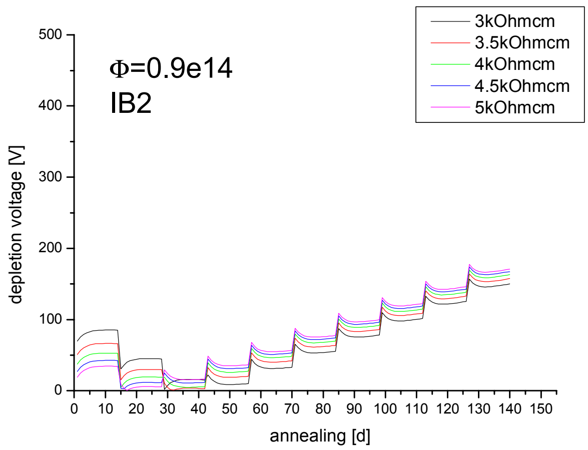

Fig. 27 : Simulation of the evolution of the depletion voltage as function of the initial resistivity, irradiation fluence and annealing time at LHC, for inner barrel CMS tracker sensor of different initial resistivities (taken from [44]).

In parallel to the issue of the depletion voltage, the sensor must have a good stability of the high voltage and must avoid breakdown. As the acceptance criterion for the depletion voltage at the end of the detector's lifetime is 300 V, the minimal voltage for stability against bulk breakdown has been set to 500V and is guaranteed by a guard ring. Small shorts between strips can occur as the field increases with overdepletion. To avoid them the metallization of the strips is designed wider than the implantation width. Since the oxide breakdown field is higher than the crystal breakdown field[¤], the metal overhang ensures a higher breakdown stability of the sensor. This will keep the S/N ratio of the modules as good as possible after irradiation.

[¤] The breakdown voltages for the silicon crystal and Silicon oxide, quoted in Table 26 and Table 27, are respectively of about 3 10^5 V/cm and between 5 and 8 10^6 V/cm.

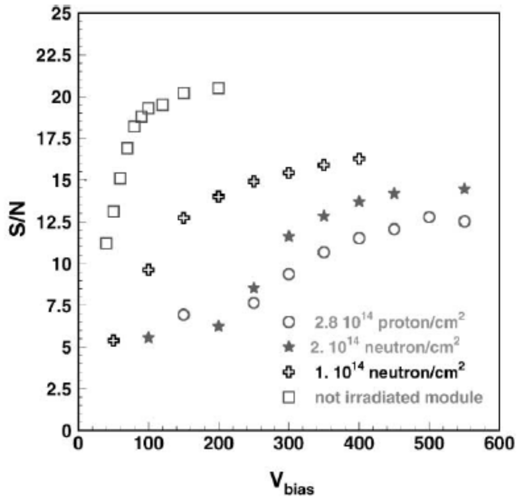

Fig. 28 : Signal to noise ration of irradiated CMS R&D structures (from [39]). The Breakdown resistance of the detector is clearly shown here as a crucial characteristic of the detector as the best ratio is obtained at high bias.

The enhancement has also proven to be better on <100> than <111>-oriented detectors, making it an additional argument for the choice of the first orientation.

In the case of CMS sensors, a rough estimation of the width of the charge cloud generated, without any magnetic field applied, is given by e.g. [2], p111.

	L1 (mm)	L2 (mm)	height (mm)	thickness (mm)
IB1	63,3	63,3	119,0	0,32
IB2	63,3	63,3	119,0	0,32
W1tec	64,6	87,9	87,2	0,32
W1tid	63,6	93,8	112,9	0,32
W2	88,2	112,2	90,2	0,32
W3	64,9	83,0	112,7	0,32
W4	59,7	73,2	117,2	0,32
OB1	96,4	96,4	94,4	0,50
OB2	96,4	96,4	94,4	0,50
W5a	98,9	112,3	84,0	0,50
W5b	112,5	122,8	66,0	0,50
W6a	86,1	97,4	99,0	0,50
W6b	97,5	107,5	87,8	0,50
W7a	74,0	82,9	109,8	0,50
W7b	82,9	90,8	90,8	0,50

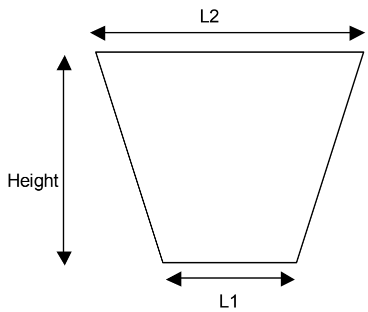

Table 3 : The different CMS sensor designs.

2.5. Qualification procedure for the CMS tracker sensors

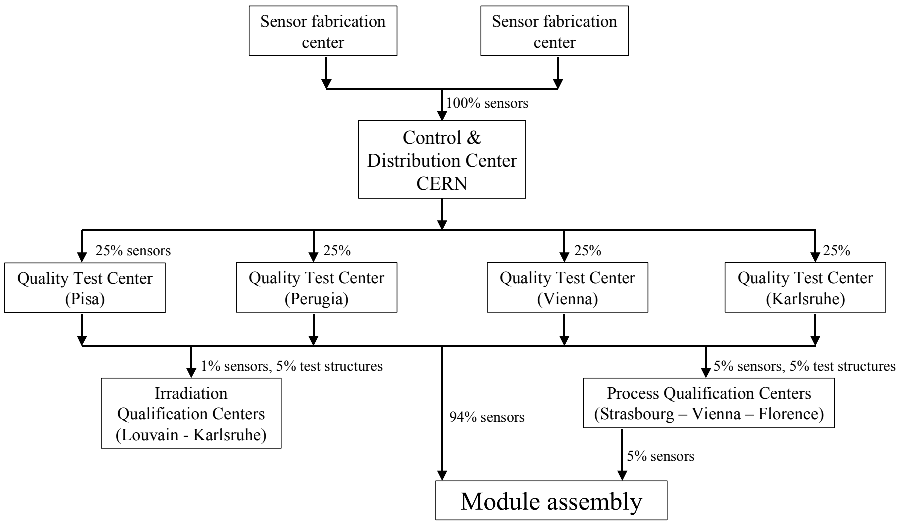

Fig. 29 : The CMS silicon sensor qualification scheme. This work is part of the tasks belonging to the Irradiation qualification centers.

The radiation hardness tests performed by the CMS silicon sensor group (cf. 3.3) are to be placed in the context of a broader quality assurance scheme to which many institutes collaborate [45]. Shown on Fig. 29, this rather complex procedure is required as the tracker will be made of several thousands of sensors and because the collaboration is expecting uniform properties of the silicon modules across the whole sub detector.

Each phase of the qualification procedure is well identified from the other ones and each institute, whether quality test center (QTC), process qualification center (PQC) or irradiation qualification center (IQC), has its own well-defined role and acceptance criteria for the different tests. Besides the sensor qualification scheme, there are also bonding tests which check that the sensors can easily be connected to the associated electronics via the pitch adapter.

	Test	Acceptance criteria
Global	IV	I_{leak} < 100 nA/cm^2 at V_{bias} = 500 V, V_{break} > 500 V
	CV	100 V < V_{dep} < 250 V
Strip by strip	Pinhole measurement	Current through dielectric less than 1 nA
	R_{poly}	Average value between 1 and 2 MΩ, with stdev < 0.3 MΩ
	Strip leakage current	I_{leak} < 500 nA
	C_{ac}	1.2 – 1.3 pF/cm/µm (normalized to the length of the strip and width of implantation)
	Total defect strips	< 1%
	(Strip parameters tested on a fraction of the strips only)	

Table 4 : Tests performed on sensors by quality test centres, and the corresponding qualification criteria (cf. [46]).

The quality test centres check the overall manufacturing quality by making full tests on a sample basis. There is in principle no need to test all sensors, but a sampling is justified as the characteristics may vary from batch to batch. In this context, the QTCs test all batches and, if these pass the tests, distribute samples of structures and sensors to the other test centres. The checks made at this level are an optical inspection of the sensors and an electrical check covering CV, IV, a strip scan to detect any pinhole and measurements of the strip leakage current, its bias resistor and coupling capacitance. The collaboration fixed acceptance criteria (cf. Table 4) on all the measured values and can reject the sensor on a basis of the CV-IV values as well as the number of defect strips.

The process qualification centres use the mini sensor and various structures built on the silicon wafer to monitor the stability of a number of parameters related to the processing of the wafer (e.g. oxide quality and breakdown characteristics, aluminium or implant resistivity, cf. Table 5). They also perform long-term stability tests.

Measurements	Acceptance criteria
CV	100 V < V_{dep} < 250 V (also depends on resistivity)
IV	I_{leak} < 100 nA/cm^2 at V_{bias} = 500 V, V_{break} > 500 V (test performed at room temp.)
C_{int}	C_{int} within 10 % of the parameterization
R_{int}	> 1 GΩ
R_{poly} R_{p+} R_{Al}	Between 1 and 2 MΩ, stdev < 0.3 MΩ < 200 kΩ/cm ≤ 18 mΩ/cm^2
C_{ac} V_{break} of C_{ac} I_{diel}	> 1.2 pF/cm/µm > 120 V < 1 nA (at 120 V)

Table 5 : Summary of the measurements and acceptance criteria for the process qualification center (PQC) tests (cf. [46]).

In parallel to the PQC tests, radiation tests are performed by the two IQCs. The latter are in fact ageing tests and hence destructive tests. For this reason, mainly test structures have been tested (5 % of the production), along with a small percentage of sensors (1 %). Dispatched over two IQC, it nevertheless corresponds to more than 120 sensors and 600 test structures for each centre. After all the improvements we made to the irradiation setup, we were able to put simultaneously 16 test structures and 4 sensors maximum in the beam per irradiation. At a rhythm of about one irradiation per month during the beam time periods of the cyclotron we tested more than 180 structures during 2004. This is however too small regarding the total amount of devices to be tested. As there was no possibility to get more beam time, it has been decided to irradiate structures from as many different batches as possible. The results and their compliance to the acceptance criteria (Table 6) have to be assessed regarding the fluence that the devices have undergone.

Therefore, the depletion voltage and leakage current are studied and compared to literature using the NIEL approximation. In this way, one can estimate the radiation hardness of the sensors by simulating the LHC environment.

Test	**Acceptance criteria**
CV	V_{dep} < 250 V (+ Hamburg model)
IV	$\alpha \sim 3.5\text{-}4.5\ 10^{-17}$ A/cm V_{break} > 500 V
I_{strip}	Detect leaky strips on a sample basis
C_{int}	< 1.2 pF/cm
C_{ac}	> 1.2 pF/cm/µm
R_{poly}	between 1 and 2 MΩ, stdev < 0.3 MΩ
R_{int}	> 20 MΩ

Table 6 : Criteria for the irradiation qualification (IQC) tests.